Systematic study of the nuclear potential diffuseness through high precision back-angle quasi-elastic scattering

M. Evers, M. Dasgupta, D. J. Hinde, L. R. Gasques,* M. L. Brown, R. Rafiei, and R. G. Thomas†
Department of Nuclear Physics, Research School of Physical Sciences and Engineering, Australian National University, Canberra, ACT 0200, Australia
(Received 4 August 2008; published 30 September 2008)

High precision measurements for back-angle quasi-elastic scattering of ^{16}O from various target nuclei have been made, and are compared with coupled channels calculations to determine the diffuseness of the real part of the Woods-Saxon nuclear potential. The extracted diffuseness parameters are in the range of 0.60 to 0.69 fm, and agree well with previous results using a ^{32}S projectile. The measured quasi-elastic energy spectra close to the barrier show both discrete peaks and a broad continuous structure with Q-values down to −25 MeV. These suggest the inadequacy of coupled channels calculations that include couplings only to low energy, discrete states of the colliding nuclei.

DOI: 10.1103/PhysRevC.78.034614 PACS number(s): 25.70.Bc, 24.10.Ht, 24.10.Eq

I. INTRODUCTION

It is generally accepted that coupled channels calculations, taking into account couplings to low-lying collective states of the target and projectile, can give good agreement with both scattering and fusion data [1,2]. However, describing scattering data requires the use of a different value of the diffuseness of the real nuclear potential compared to fusion data [3,4], which might point to inadequacies in the current treatment of near-barrier reactions [4].

Precise measurements of sub-barrier quasi-elastic scattering have recently been recognized [5–8] as a new tool for the determination of the shape of the real part of the nuclear potential in the surface region. The sensitivity of back-angle quasi-elastic scattering to the nuclear potential can be readily understood in a classical picture. The introduction of an attractive nuclear potential V_N in addition to the Coulomb potential V_C between target and projectile leads to deflection of the classical Rutherford trajectories to more forward angles, and hence results in a reduction of scattered flux at a fixed backward angle. However, other processes may also result in modification of the reflected flux. Depending on the incident energy of the projectile, couplings to intrinsic states in both the target and projectile, that can occur at large distances, as well as (multi)nucleon transfer reactions, may result in a further deflection from the classical Rutherford trajectories. As the energy increases toward the fusion barrier V_B, fusion will start to occur, resulting in a drastic removal of flux at backward angles.

In this paper, precision measurements of quasi-elastic scattering at far-backward angles are presented, using beams of ^{16}O at energies below the fusion barrier. A consistent analysis of these data was performed using coupled channels calculations, carried out with a version of the code CCFULL [9], modified to calculate quasi-elastic yields. The back-angle energy spectra at beam energies closest to V_B show the presence of many more exit channels than are included in the calculations, having more negative Q-values, but with as high or higher reaction yields than those of the included channels. This observation raises questions about the adequacy of the standard application of coupled channels calculations of both fusion and scattering.

II. EXPERIMENTAL METHOD

The experiments were carried out using beams of ^{16}O from the 14UD tandem electrostatic accelerator at the Australian National University. The targets, with thicknesses between 50 and 200 μg/cm^2, evaporated on to 15–20 μg/cm^2 C backings, were mounted perpendicular to the beam axis. Measurements were conducted in two different runs, using two slightly different detector configurations. An annular Si surface barrier detector, placed at a mean laboratory angle of $\theta_{\rm lab} = 174^\circ$ to the beam axis, was used during the first run. The energy spectra obtained had a background of around 30 counts per channel (for typically 10^5 counts per channel at the elastic peak). Due to the proximity of the annular detector to the beam axis, the background may have resulted from backscattering from the beam dump located downstream of the scattering chamber. To minimize these background events, in the second run a Si detector (ion implanted) was placed away from the beam axis, at a mean angle $\theta_{\rm lab} = 163^\circ$. This setup reduced the background events in the spectra to about 8 to 10 counts per channel for the same 10^5 counts per channel at the elastic peak. In both runs two Si surface barrier detectors (monitors) were placed symmetrically around the beam axis at angles of $\pm 30^\circ$, and were used to measure Rutherford scattering events for normalization. The details of the different experimental setups, together with the various targets that were investigated during the two runs, are summarized in Table I.

The main goal of the experimental procedure was to obtain quasi-elastic scattering cross section data with very high

*Permanent address: Centro de Física Nuclear da Universidade de Lisboa, Lisbon, Portugal.

†Permanent address: Bhabha Atomic Research Centre, Mumbai, India.

TABLE I. Details for the two experiments. θ_{lab} is the mean scattering angle of the detector. The thin rare earth targets become oxidised after evaporation.

	Back-angle detector	θ_{lab}	Targets
Run 1	Annular surface barrier detector	174°	$^{144,154}SmO_x$, $^{166}ErO_x$, ^{186}W, ^{197}Au, ^{208}PbS
Run 2	Implanted Si detector	163°	$^{144}SmO_x$, ^{208}PbS

precision (uncertainties <1%). To minimize systematic errors, the following measurement procedures were adopted:

(i) Degradation of both the detector response and the target material during the experiment could lead to systematic errors. Thus the measurements were not conducted in ascending or descending order of beam energy. Instead, they were performed by tuning energies semirandomly, choosing the beam charge state to ensure that the current in the analyzing magnet (which selects the beam energy) increased monotonically with every successive measurement. The latter procedure minimized differential hysteresis effects in the analyzing magnet [10].

(ii) For fragile targets, or those with a low melting point (^{144}Sm, ^{166}Er, ^{208}Pb), the target ladder was moved in small steps by ±2 mm with a 20 s period during the individual measurements, to distribute the effects of target heating and radiation damage over a larger area of the target.

(iii) To maintain the same focal point of the incident beam particles on the target, the ^{16}O beam was focused through a circular aperture with a diameter of 2 mm, located on the target ladder, prior to every measured energy.

(iv) The scattering events in the backward angle detector were corrected for electronic dead time using a pulser signal injected into the preamplifier. Dead times were much smaller than 1% for the count rates of ∼300 Hz that were maintained throughout the measurements.

III. RESULTS AND ANALYSIS

Typical fragment yields as a function of the Q-value are shown in Fig. 1 for the reaction ^{16}O+^{208}Pb at three different energies. These show both the elastic peak and a number of discrete reaction channels, which become more prominent at the higher bombarding energies. The back-angle quasi-elastic events were selected by defining an energy window for each spectrum to include both the elastic peak and all quasi-elastic events at lower energies. The total number of counts, after subtraction of the background (the latter corresponds to typically 1% of the total number of counts in the chosen energy window), was divided by the sum of the elastic counts in the two monitors at forward angles to obtain the ratio of quasi-elastic to Rutherford scattering cross sections $d\sigma_{qel}/d\sigma_{Ruth}$. Variations in the axial position of the different targets, originating from variations of the target mounting and planarity, can give rise to differences in the normalization factor of $d\sigma_{qel}/d\sigma_{Ruth}$ between the various targets. Every target was therefore analyzed independently, resulting in slightly different normalization factors for each reaction [see Eq. (3)]. At the lowest beam energies for all targets, the Q-value spectra showed no peaks for $Q < 0$, indicating an absence of any significant target impurities at a level of ∼100 ppm.

The excitation functions for quasi-elastic scattering for each reaction measured in this work are shown in Fig. 2. Error bars of the data points (resulting only from statistical uncertainties) are generally very small, and by using the aforementioned measurement procedure, the scatter in the quasi-elastic scattering data for each target was minimized. The larger scatter in the data for the ^{144}Sm target will be discussed below, after the steps taken to obtain the diffuseness parameter through comparison with coupled channels calculations are described.

A. Potential parameters

The single channel and coupled channels calculations were carried out using a Woods-Saxon parametrization of the nuclear potential with an internal (volume) imaginary potential

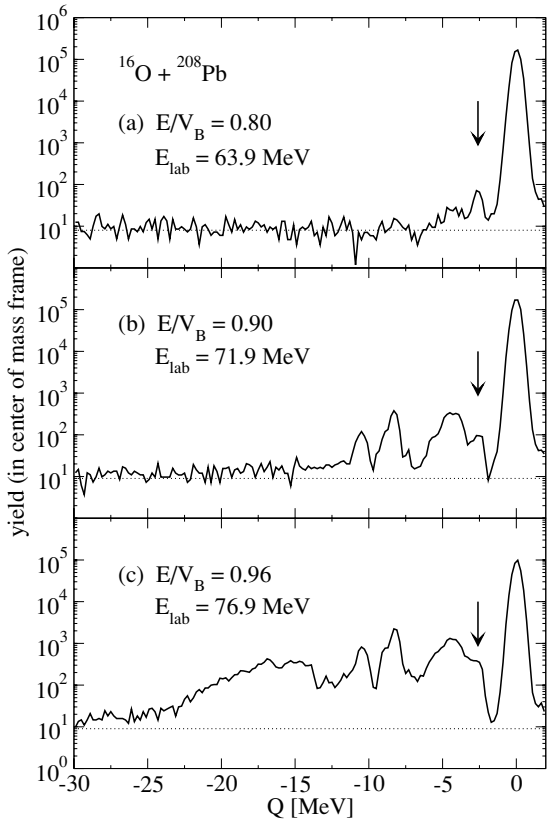

FIG. 1. Energy spectra measured in the backward-angle detector at $\theta_{lab} = 163°$ for the reaction ^{16}O+^{208}Pb at the indicated energies. The dotted line shows the background, the arrows indicate the peak resulting from excitation of the 3^- state at 2.614 MeV in ^{208}Pb.

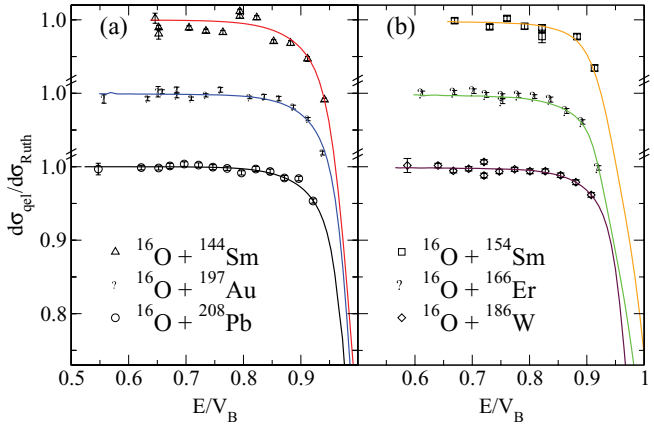

FIG. 2. (Color online) Ratio of the experimental quasi-elastic to Rutherford scattering cross sections $d\sigma_{\rm qel}/d\sigma_{\rm Ruth}$ for all reactions studied in this work, shown for (a) (near-)spherical and (b) non-spherical target nuclei. Cutoffs of $E/V_B \leqslant 0.94$ and $E/V_B \leqslant 0.93$, respectively, for the spherical and non-spherical targets were used for the coupled channels model analyses (see text), and only the data points up to these limits are shown.

to account for the small absorption at sub-barrier energies following barrier penetration:

$$V_N(r) = -\frac{V_0}{1+\exp\frac{r-R_0}{a_0}} - i\frac{W}{1+\exp\frac{r-R_W}{a_W}}, \qquad (1)$$

with the radii of the real and imaginary part given by

$$R_{0,W} = r_{0,W}\left(A_p^{1/3} + A_t^{1/3}\right) \qquad (2)$$

for the target and projectile nuclei with masses A_t and A_p, respectively.

The values used for the parameters of the imaginary potential ($W = 30.0$ MeV, $r_W = 0.8$ fm, $a_W = 0.10$ fm) result in negligible strength in the surface region, thus the quasi-elastic scattering cross section was insensitive to reasonable variation of the imaginary potential parameters. To guarantee that every parameter set of the real part of the Woods-Saxon potential (V_0, r_0, a_0), used in the calculations gave the correct empirical fusion barrier energy V_B, the following procedure was adopted (also shown in Fig. 3).

(i) For a chosen and fixed diffuseness value a_0, and with $r_0 = 1$ fm, the potential depth V_0 is determined such that the fusion barrier energy V_B, known experimentally for all but two systems (see Table II), is correctly reproduced.

(ii) The single channel fusion cross sections $\sigma_{\rm fus}^{\rm sc}$ are calculated.

(iii) The full coupled channels fusion cross sections $\sigma_{\rm fus}^{\rm cc}$ are then calculated. In general these are different from $\sigma_{\rm fus}^{\rm sc}$ due to potential renormalization [11,12]. By slightly adjusting the radius r_0, the fusion cross sections $\sigma_{\rm fus}^{\rm cc}$ at energies well above the barrier were matched with the single channel fusion cross sections $\sigma_{\rm fus}^{\rm sc}$. This results in a set of potential parameters (V_0, r_0, a_0) that reproduces the fusion barrier taking into account the couplings to the intrinsic states that are included in the coupled channels calculations.

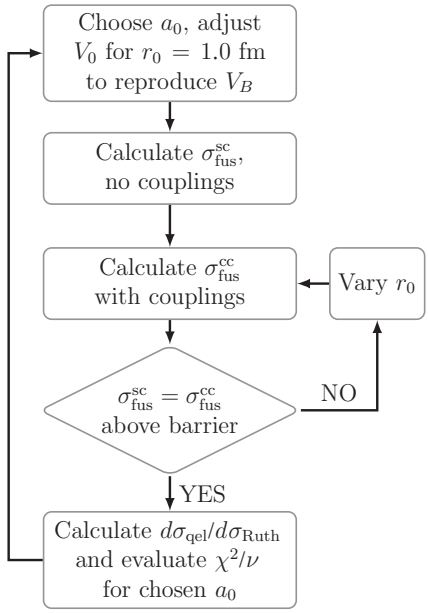

FIG. 3. Summary of the data fitting routine which ensures that the fusion barrier energy is correctly reproduced by every parameter set of the real Woods-Saxon nuclear potential.

(iv) For every set of nuclear potential parameters, both for the single channel and coupled channels analyses, the χ^2 per degree of freedom ν between the experimental quasi-elastic scattering data and the coupled channels calculations is calculated as

$$\frac{\chi^2}{\nu} = \frac{1}{\nu}\sum_{i=1}^{n}\frac{\left[N\left(\frac{d\sigma{\rm qel}}{d\sigma{\rm Ruth}}\right)_{i,\rm exp} - \left(\frac{d\sigma{\rm qel}}{d\sigma{\rm Ruth}}\right)_{i,\rm calc}\right]^2}{\delta_i^2}. \qquad (3)$$

Here the normalization constant N is a free parameter and $\nu = n - k$, where n is the total number of quasi-elastic data points for each reaction and k is the total number of free parameters. The δ_i denote the assigned uncertainties for each experimental data point.

(v) A different value of a_0 is chosen, and steps one to four are repeated, to obtain the χ^2/ν envelope, and thus the value of a_0 giving the best fit to the data.

The derived a_0 values are not sensitively dependent on the choice of r_0. Varying r_0 by 10% changes the best-fitting value

TABLE II. Fusion barrier energies V_B used to constrain the real nuclear potential parameters.

Reaction	V_B [MeV]	Source
$^{16}O+^{144}Sm$	61.10 ± 0.05	Ref. [10]
$^{16}O+^{154}Sm$	59.40 ± 0.05	Ref. [10]
$^{16}O+^{166}Er$	64.99	scaled from $^{16}O+^{186}W$ data
$^{16}O+^{186}W$	68.9 ± 0.06	Ref. [10]
$^{16}O+^{197}Au$	72.58	scaled from $^{16}O+^{186}W$ data
$^{16}O+^{208}Pb$	74.5 ± 0.05	Ref. [13]

for a_0 by 0.03 fm, which is similar to the uncertainties in a_0 resulting from experimental uncertainties.

The experimental fusion barrier energies were taken from experiments [10,13], or were scaled from neighboring reactions using the Coulomb scaling factor $Z_p Z_t/(A_p^{1/3} + A_t^{1/3})$, and are summarized in Table II. It is important to note that the best fit diffuseness parameter is not very sensitive to the fusion barrier energy, a variation of ± 0.5 MeV in the barrier energy results in a difference in the diffuseness parameter of ± 0.02 fm, which is again of the same order as the uncertainties in a_0 from the fitting procedure. This can be understood from the weak energy dependence of the $d\sigma_{\rm qel}/d\sigma_{\rm Ruth}$ at sub-barrier energies, as seen in Fig. 2.

B. Coupling parameters

The deformation parameter β_λ associated with a transition of multipolarity λ in a nucleus with charge Z was obtained from experimental electromagnetic transition probabilities $B(E\lambda)\uparrow$ using [14]:

$$\beta_\lambda = \frac{4\pi}{3ZeR^\lambda} M(E\lambda), \tag{4}$$

where the matrix element $M(E\lambda)$ satisfies

$$B(E\lambda)\uparrow = |M(E\lambda)|^2. \tag{5}$$

The radius of the nucleus is taken to be $R = r_{\rm nuc} A^{1/3}$, using the standard value for $r_{\rm nuc}$ of 1.20 fm. The effect of using a smaller value for $r_{\rm nuc}$ on the determination of the diffuseness parameter will be discussed later. Experimental $B(E2)\uparrow$ values were taken from [14], $B(E3)\uparrow$ values from [15,16], and $B(E4)\uparrow$ values for ^{154}Sm and ^{186}W from [17] and [18], respectively. For ^{197}Au, interpolated values from neighboring even-even nuclei were used [7].

For the ^{16}O projectile, the coupling to the first 3^- state at $E = 6.130$ MeV was found to have a negligible effect on the determination of the diffuseness parameter. Hence ^{16}O was treated as inert in the coupled channels calculations for all reactions studied here. The coupling parameters of the target nuclei for all the reactions studied here are summarized in Table III

TABLE III. Coupling parameters used in the calculations. E_x denotes the energy of the first excited state (2^+) of the ground-state rotational band for rotational nuclei, and the energy of the vibrational phonon state with angular momentum and parity J^π for vibrational nuclei. (β_2, β_4) and β denote the deformation parameters within the rotational and vibrational models, respectively. $N_{\rm rot}$ and $N_{\rm ph}$ are the number of rotational states and the number of vibrational phonons considered in the coupled channels calculations. For ^{208}Pb the double-octupole excitation was included, as well as all mutual couplings of excited vibrational states.

Rotational nuclei				
Nucleus	E_x [MeV]	β_2	β_4	$N_{\rm rot}$
^{154}Sm	0.0820	0.341	0.05	5
^{166}Er	0.0806	0.342	0.007	5
^{186}W	0.1226	0.224	−0.08	5
^{197}Au	0.384[a]	0.117[a]	0.0	3
Vibrational nuclei				
Nucleus	E_x [MeV]	J^π	β	$N_{\rm ph}$
^{144}Sm	1.660	2^+	0.088	1
	1.8102	3^-	0.13	1
^{208}Pb	2.614	3^-	0.11	2
	3.197	5^-	0.06	1

[a]Average of neighboring nuclei, see text.

C. Fitting data

The quasi-elastic scattering analyses should be restricted to energies at which absorption due to fusion is minimal. This ensures that the extracted potential diffuseness parameter is independent of whether the coupled channels calculations exactly reproduce the experimentally measured fusion cross sections. According to Ref. [6], and as applied in Ref. [7], the quasi-elastic scattering analyses should be restricted to values of $d\sigma_{\rm qel}/d\sigma_{\rm Ruth} > 0.94$, which for the reactions studied here, corresponds on average to $E/V_B \leqslant 0.95$. During this experiment scattering cross sections were measured at energies closer to the fusion barrier, up to $E/V_B \sim 0.97$, hence the effect of excluding high energy data points on the determination of the diffuseness parameter could be investigated. This was done by extracting the diffuseness parameter when successively omitting the highest energy point from the data set. The results in Fig. 4 show the best-fitting diffuseness parameter a_0 as a function of the cut-off value of E/V_B for the two reactions ^{16}O+^{208}Pb and ^{16}O+^{186}W. The a_0 value is progressively better defined and converges as more data points are included. However for ^{16}O+^{186}W, as absorption becomes significant, for $E/V_B \geqslant 0.94$, the extracted diffuseness shows a rise. This occurs because a larger a_0 value mimics the effect of absorption by effectively lowering the quasi-elastic yield. As a result of this analysis a consistent procedure was adopted to include data points with $E/V_B \leqslant 0.94$ for all reactions involving spherical targets and $E/V_B \leqslant 0.93$ for all reactions with non-spherical target nuclei. The difference in the cut-off E/V_B value can be understood in terms of the coupled channels picture, where the couplings to intrinsic states lead to a significantly wider fusion barrier distribution for deformed nuclei [19,20], whereas those involving spherical nuclei are less affected by couplings, resulting in a higher energy cutoff.

1. Spherical target nuclei

The experimental data points for the ^{144}Sm reaction analysis show a considerably larger scatter than for any other reaction (see Fig. 2). This is emphasized by the large number of counts obtained at each energy (up to 2×10^5 counts), which results in very small statistical error bars. The reason for the scatter in the ^{16}O+^{144}Sm data is unclear. Non-planarity of the target leads to areas on the target with slightly different axial positions with respect to the beam axis z. A difference of z as small as 0.5 mm results in a change of the normalization factor by ∼1.5%, which is similar to the observed scatter in the data. However, there is no correlation between the deviation from

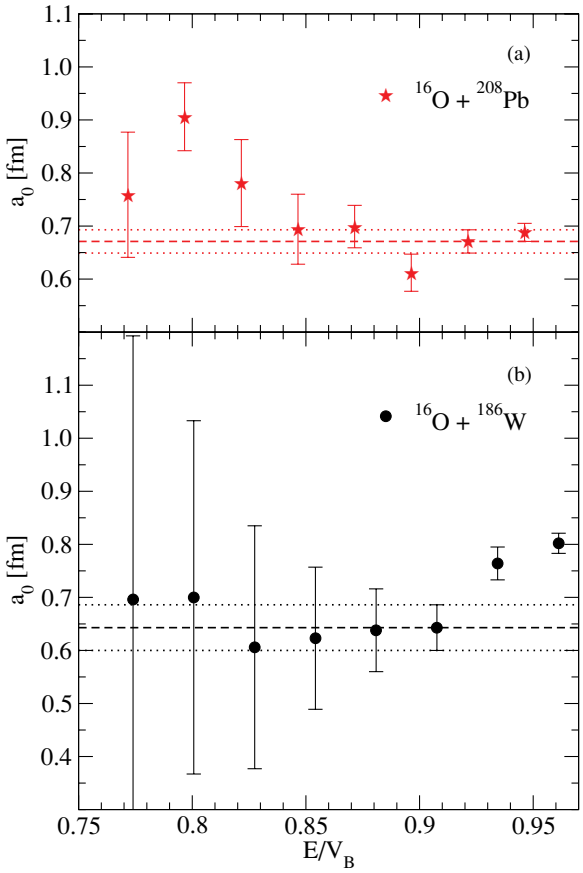

FIG. 4. (Color online) Best fit diffuseness parameter as a function of the highest energy point (cutoff) included in the fitting routine for the two reactions (a) ^{16}O+^{208}Pb and (b) ^{16}O+^{186}W. The dashed line shows the adopted diffuseness parameter, whose uncertainty is indicated by the two dotted lines.

the fit and the sequence of the measurements during the experiment. Thus we can only suggest fluctuating distortions of the target due to radiation damage as a possible explanation.

For the reaction ^{16}O+^{144}Sm, couplings to the quadrupole and octupole phonon states in ^{144}Sm together with their mutual interactions were included, with coupling parameters given in Table III. In ^{208}Pb, couplings to the 3^-, 5^-, and double octupole ($3^- \otimes 3^-$) phonon states (Table III), as well as all mutual couplings were included.

2. *Non-spherical target nuclei*

For the near-spherical target nucleus ^{197}Au rotational couplings were included with parameters given in Table III, which were determined by averaging the values for β_2 and the energies of the first excited rotational 2^+ states in the neighboring ^{196}Pt and ^{198}Hg nuclei. In the coupled channels calculations, couplings to the first, second and third member of the ground-state rotational band were considered, after checking that the inclusion of higher rotational states does not change the calculated quasi-elastic scattering cross sections. Couplings to the fourth and fifth rotational states were found to lead to numerical instabilities in the coupled channels code CCFULL, resulting in erratic fluctuations of the quasi-elastic scattering cross section, though only at energies $E/V_B < 0.76$.

For the well-deformed target nuclei ^{154}Sm, ^{166}Er, and ^{186}W, couplings up to the fifth rotational state were included. The coupling parameters for the three reactions are summarized in Table III. It was found that couplings to intrinsic states play a significant role in the determination of the diffuseness of the nuclear potential, as coupled channels calculations require a significantly smaller diffuseness parameter to describe the experimental data (see Table IV).

To check for any dependence of the best fit diffuseness parameter on the value of $r_{\rm nuc}$, a coupled channels analysis was performed for the reaction ^{16}O+^{166}Er, using a value of $r_{\rm nuc} = 1.06$ fm [10], for which the calculated deformation parameters are $\beta_2 = 0.438$, $\beta_4 = 0.011$. The diffuseness parameter was found to be smaller by only 0.002 fm, and hence it was concluded that the extracted diffuseness parameter is insensitive to variation of $r_{\rm nuc}$, in agreement with the conclusion of Ref. [7].

D. Experimental diffuseness parameter

The best fits to the measured quasi-elastic scattering differential cross sections using the coupled channels analysis are shown in Fig. 2. The diffuseness parameters a_0 obtained from the best fits, with and without couplings are summarized in Table IV. The uncertainties in a_0 were calculated according to the following procedure [21]. Using the $\chi^2_{\rm min}$ value corresponding to the best fit value of the diffuseness parameter, the quantity

$$\hat{\chi}^2 = \chi^2_{\rm min} + \frac{\chi^2_{\rm min}}{\nu}, \tag{6}$$

was calculated, where ν denotes the number of degrees of freedom. The intersection of $\hat{\chi}^2$ with the χ^2 envelope gives the two values a_0^-, a_0^+, as shown in Fig. 5, resulting in an error

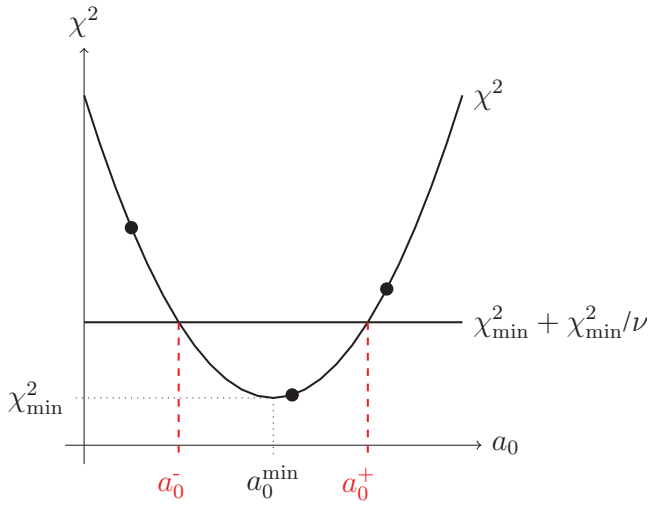

FIG. 5. (Color online) Illustration of the determination of the uncertainties for the diffuseness parameter. $\chi^2_{\rm min}$ is the χ^2 value corresponding to the best fit value for a_0, ν corresponds to the number of degrees of freedom.

TABLE IV. Best fit diffuseness parameters a_0 extracted from the single channel and coupled channels calculations (with associated V_0, r_0 values), together with χ^2 per degree of freedom of the best fit.

Reaction	Single channel				Coupled channels			
	V_0 [MeV]	r_0 [fm]	a_0 [fm]	$\chi^2_{\min}/\nu$	V_0 [MeV]	r_0 [fm]	a_0 [fm]	$\chi^2_{\min}/\nu$
^{16}O+^{144}Sm	304.7	1.0	0.745 ± 0.050	15.10	416.9	0.997	0.693 ± 0.052	14.68
^{16}O+^{154}Sm	346.7	1.0	0.762 ± 0.044	2.57	1124.3	0.998	0.603 ± 0.015	2.08
^{16}O+^{166}Er	182.7	1.0	0.881 ± 0.033	5.67	518.9	0.998	0.679 ± 0.012	1.36
^{16}O+^{186}W	638.5	1.0	0.685 ± 0.040	2.92	884.7	0.999	0.643 ± 0.043	2.89
^{16}O+^{197}Au	673.0	1.0	0.685 ± 0.023	3.14	828.4	1.001	0.656 ± 0.010	2.59
^{16}O+^{208}Pb	901.4	1.0	0.664 ± 0.021	1.27	853.0	0.993	0.671 ± 0.022	1.25

for a_0 of

$$\Delta a_0 = \frac{a_0^+ - a_0^-}{2}. \quad (7)$$

Single channel fits to the quasi-elastic scattering data give diffuseness parameters between $a_0 = 0.66$ and 0.88 fm, while coupled channels analyses lead to values for a_0 in the narrower range of $a_0 = 0.60$ to 0.69 fm. As was expected [7] in the energy regime studied here, coupled channels effects play a minor role in the best fit value for the diffuseness parameter for spherical and near-spherical nuclei, whereas couplings to rotational states reduce the value of the best-fitting diffuseness parameter significantly for reactions involving deformed target nuclei. In particular, the influence of couplings on quasi-elastic scattering is more pronounced for the reactions ^{16}O+^{154}Sm and ^{16}O+^{166}Er, where both target nuclei have a large quadrupole deformation. Once again, this can be understood in a classical picture, where the influence of the nuclear potential can be extended to lower energies by the static deformation. The larger the deformation, the lower the energy where the nuclear potential of the aligned deformed nucleus can affect the trajectories. Figure 6 shows the best-fitting values for the diffuseness parameter as a function of the mass number of the target nucleus for all reactions studied in this work. Also included are the results from Ref. [7], where a ^{32}S beam was used. The weighted average of the diffuseness values for the reactions involving ^{16}O yields $\bar{a}_0 = 0.65$ fm, which is in good agreement with results from the previous analysis with a ^{32}S beam [7], for which $\bar{a}_0 = 0.67$ fm, and for the ^{58}Ni+^{58}Ni reaction, where $\bar{a}_0 = 0.62$ fm [8]. Thus, the average value of diffuseness obtained from quasi-elastic scattering data agrees with the accepted value of ~0.63 fm [22].

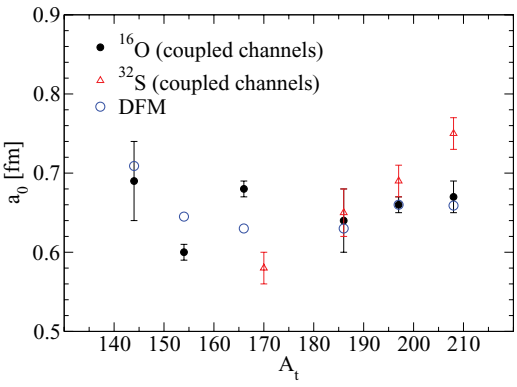

FIG. 6. (Color online) Best-fitting values for the diffuseness parameter a_0 as a function of the mass number of the target nucleus, A_t, extracted from the coupled channels analysis. The analogous results from Ref. [7], for a ^{32}S beam, are shown by open triangles. The diffuseness values from a Woods-Saxon fit to double folding model calculations (DFM) [12,23] are shown by open circles.

However, as seen from Fig. 6, there are variations in a_0 as a function of A_t. These could be associated with differences in the matter distributions. To investigate this point, the results of the present measurements are compared with results [12,23] of calculations using the double folding model, fitted with a Woods-Saxon potential [12] in the surface region. These diffuseness values are denoted by DFM in the figure. The DFM calculations show a similar trend to the current measurements, suggesting that at least some of the variation from system to system is not associated with experimental uncertainties.

IV. BACK-ANGLE QUASI-ELASTIC ENERGY SPECTRA

The extraction of the diffuseness of the real nuclear potential makes use of the integrated quasi-elastic yield; in this procedure, it is implicit that all channels not included in the calculations follow the same trajectory as those which are included. Because of the high statistics obtained in the measurements (typically 10^5, and up to 10^6 counts), the energy spectra give information on all significant non-elastic channels that are present.

In order to identify structures in the back-angle energy spectra, the measured kinetic energies of the projectile-like fragments were transformed to give the Q-values, where $Q = 0$ MeV corresponds to elastic scattering. The Q-value of a scattering reaction was calculated using the standard scattering formulas given in Ref. [24]:

$$Q = \frac{A_t + A_p}{A_t} E_3 - \frac{A_t - A_p}{A_t} E_1 - \frac{2A_p\sqrt{E_1 E_3}}{A_t} \cos\theta_{\text{lab}}, \quad (8)$$

where E_1 (E_3) denote the incoming (outgoing) energy of the projectile before (after) the scattering process in the laboratory frame, corrected for energy losses in the target material. Since the energy spectra give no information on possible mass transfer, no mass exchange was assumed in calculating the Q-value spectra. For (the more likely) stripping reactions, the deduced Q-values change by only ~ -0.5 MeV per mass unit. This small shift does not affect the following discussions

and conclusions. The yield was also transformed into the center-of-mass frame according to Ref. [24].

Examples of the resulting Q-value spectra are shown in Fig. 1 for the reaction ^{16}O+^{208}Pb, down to a Q value of -30 MeV. At bombarding energies well below the fusion barrier ($E/V_B = 0.80$), only peaks corresponding to elastic scattering ($Q = 0$) and to the first excited state in ^{208}Pb (3^- state at 2.614 MeV) are clearly visible. With increasing beam energy, the spectra develop a large number of peaks. At $E/V_B = 0.90$, states with Q values between $Q = -4$ and -15 MeV are populated, some with $\sim$0.1% of the strength of the elastic peak, which is larger than the strength of populating the 3^- state in ^{208}Pb. The energies of some of these states appear consistent with transfer reactions. By $E/V_B \sim 0.96$, these channels dominate over the 3^- state. Also seen here is a broad and more continuous structure at Q-values < -15 MeV, which is present at similar E/V_B for the other targets. The presence of this component does not significantly affect the extracted diffuseness values. This can be seen from Fig. 4, where an energy cut-off corresponding to $E/V_B = 0.90$ (below which the component essentially does not contribute) leads to the same extracted diffuseness within experimental errors. The importance of transfer in quasi-elastic scattering for heavier projectiles was highlighted in Ref. [25], and these spectra indicate that it may also play a significant role for lighter projectiles. The structure below -15 MeV could result from processes which are a doorway to dissipative energy losses which could affect fusion. Experiments are currently underway to understand the nature of these channels.

V. SUMMARY

High precision back-angle scattering energy spectra have been measured for the reactions of ^{16}O with ^{144,154}Sm, ^{166}Er, ^{186}W, ^{197}Au, and ^{208}Pb. By comparing the extracted quasi-elastic scattering cross sections with coupled channels calculations, the diffuseness of the real nuclear potential was determined for all reactions. Confirming the result of Ref. [7], it was found that in reactions with well-deformed nuclei couplings play a significant role in the description of the experimental scattering cross section data. The (weighted) average of the extracted diffuseness parameters, $\bar{a}_0 = 0.65$ fm, is consistent with the value determined from a similar analysis of reactions with a ^{32}S projectile [7]. The scatter of the diffuseness values as a function of A_t show a similar trend to DFM calculations [12,23]. Reaction Q-value spectra show many more populated channels, with more negative Q-values, yet having as high or higher yields than those of the states included in the coupled channels calculations. The complexity of the measured Q-value spectra, having low energy peaks and a broad high energy structure, suggests that a truncated coupled channels description, using a very limited number of basis states, will become increasingly poor at energies near and above the fusion barrier. Thus, both experimental and theoretical efforts are needed to understand the effect of these additional channels on the reaction processes, and to develop a complete theoretical framework including both coherent quantum aspects (described by the coupled channels approach) and classical or semi-classical [25] phenomena.

ACKNOWLEDGMENTS

The authors acknowledge the financial support of an Australian Research Council Discovery Grant. The authors would like to thank J. A. Tostevin for discussions and critical reading of the manuscript, and I. I. Gontchar for providing DFM calculations.

[1] B. Sahu, G. S. Mallick, B. B. Sahu, S. K. Agarwalla, and C. S. Shastry, Phys. Rev. C **77**, 024604 (2008).
[2] Z. F. Muhammad, K. Hagino, S. Mitsuoka, and H. Ikezoe, Phys. Rev. C **77**, 034604 (2008).
[3] A. Mukherjee, D. J. Hinde, M. Dasgupta, K. Hagino, J. O. Newton, and R. D. Butt, Phys. Rev. C **75**, 044608 (2007).
[4] J. O. Newton, R. D. Butt, M. Dasgupta, D. J. Hinde, I. I. Gontchar, C. R. Morton, and K. Hagino, Phys. Rev. C **70**, 024605 (2004).
[5] K. Hagino, T. Takehi, A. B. Balantekin, and N. Takigawa, Phys. Rev. C **71**, 044612 (2005).
[6] K. Washiyama, K. Hagino, and M. Dasgupta, Phys. Rev. C **73**, 034607 (2006).
[7] L. R. Gasques, M. Evers, D. J. Hinde, M. Dasgupta, P. R. S. Gomes, R. M. Anjos, M. L. Brown, M. D. Rodríguez, R. G. Thomas, and K. Hagino, Phys. Rev. C **76**, 024612 (2007).
[8] D. J. Hinde, R. L. Ahlefeldt, R. G. Thomas, K. Hagino, M. L. Brown, M. Dasgupta, M. Evers, L. R. Gasques, and M. D. Rodriguez, Phys. Rev. C **76**, 014617 (2007).
[9] K. Hagino, N. Rowley, and A. T. Kruppa, Comput. Phys. Commun. **123**, 143 (1999).
[10] J. R. Leigh, M. Dasgupta, D. J. Hinde, J. C. Mein, C. R. Morton, R. C. Lemmon, J. P. Lestone, J. O. Newton, H. Timmers, J. X. Wei *et al.*, Phys. Rev. C **52**, 3151 (1995).
[11] K. Hagino, N. Takigawa, and S. Kuyucak, Phys. Rev. Lett. **79**, 2943 (1997).
[12] I. I. Gontchar, D. J. Hinde, M. Dasgupta, and J. O. Newton, Phys. Rev. C **69**, 024610 (2004).
[13] C. R. Morton, A. C. Berriman, M. Dasgupta, D. J. Hinde, J. O. Newton, K. Hagino, and I. J. Thompson, Phys. Rev. C **60**, 044608 (1999).
[14] S. Raman, C. H. Malarkey, W. T. Milner, C. W. Nestor, Jr., and P. H. Stelson, At. Data Nucl. Data Tables **36**, 1 (1987).
[15] R. H. Spear, At. Data Nucl. Data Tables **42**, 55 (1989).
[16] T. Kibedi and R. H. Spear, At. Data Nucl. Data Tables **80**, 35 (2002).
[17] J. R. Leigh, N. Rowley, R. C. Lemmon, D. J. Hinde, J. O. Newton, J. X. Wei, J. C. Mein, C. R. Morton, S. Kuyucak, and A. T. Kruppa, Phys. Rev. C **47**, R437 (1993).
[18] I. Y. Lee, J. X. Saladin, J. Holden, J. O'Brien, C. Baktash, C. Bemis, P. H. Stelson, F. K. McGowan, W. T. Milner, J. L. C. Ford *et al.*, Phys. Rev. C **12**, 1483 (1975).
[19] M. Dasgupta, D. J. Hinde, N. Rowley, and A. M. Stefanini, Annu. Rev. Nucl. Part. Sci. **48**, 401 (1998).

[20] N. Rowley, G. R. Satchler, and P. H. Stelson, Phys. Lett. **B254**, 25 (1991).

[21] P. McCullagh and J. A. Nelder, *Generalized Linear Models, Second Edition (Monographs on Statistics and Applied Probability)* (Chapman & Hall/CRC, Boca Raton, FL, 1989), 2nd ed., ISBN 9780412317606, p. 126.

[22] R. A. Broglia and A. Winther, *Heavy Ion Reactions (Lecture Notes), Volume 1: Elastic and Inelastic Reactions* (Benjamin/Cummings Publishing Company, Inc., San Francisco, CA, 1981), ISBN 0805313028, p. 114.

[23] I. I. Gontchar, D. J. Hinde, M. Dasgupta, C. R. Morton, and J. O. Newton, Phys. Rev. C **73**, 034610 (2006).

[24] J. B. Marion and F. C. Young, *Nuclear Reaction Analysis (Graphs and Tables)* (North-Holland Pub. Co, Amsterdam, 1968), ISBN B0006BUORM, pp. 141,142.

[25] G. Pollarolo, Phys. Rev. Lett. **100**, 252701 (2008).